SHAPE AND STRESS SENSING
OF MULTILAYERED COMPOSITE AND SANDWICH STRUCTURES
USING AN INVERSE FINITE ELEMENT METHOD

PRISCILLA CERRACCHIO[*], MARCO GHERLONE[*], MARCO DI SCIUVA[*] AND ALEXANDER TESSLER[†]

[*] Department of Mechanical and Aerospace Engineering, Politecnico di Torino
Corso Duca degli Abruzzi 24, 10129 Torino, Italy
e-mail: {priscilla.cerracchio, marco.gherlone, marco.disciuva}@polito.it, web: www.aesdo.polito.it

[†] Structural Mechanics and Concepts Branch, NASA Langley Research Center
Mail stop 190, Hampton, Virginia 23681-2199, U.S.A
email: Alexander.tessler-1@nasa.gov, web: www.nasa.gov

Key words: Composite Structures, Sandwich Structures, Shape Sensing, Stress Sensing, Inverse Finite Element Method, Inverse Plate Element.

Abstract. The marked increase in the use of composite and sandwich material systems in aerospace, civil, and marine structures leads to the need for integrated Structural Health Management systems. A key capability to enable such systems is the real-time reconstruction of structural deformations, stresses, and failure criteria that are inferred from in-situ, discrete-location strain measurements. This technology is commonly referred to as *shape- and stress-sensing*. Presented herein is a computationally efficient shape- and stress-sensing methodology that is ideally suited for applications to laminated composite and sandwich structures. The new approach employs the inverse Finite Element Method (iFEM) as a general framework and the Refined Zigzag Theory (RZT) as the underlying plate theory. A three-node inverse plate finite element is formulated. The element formulation enables robust and efficient modeling of plate structures instrumented with strain sensors that have arbitrary positions. The methodology leads to a set of linear algebraic equations that are solved efficiently for the unknown nodal displacements. These displacements are then used at the finite element level to compute full-field strains, stresses, and failure criteria that are in turn used to assess structural integrity. Numerical results for multilayered, highly heterogeneous laminates demonstrate the unique capability of this new formulation for shape- and stress-sensing.

1 INTRODUCTION

The inverse problem of shape- and stress-sensing is manifested by reconstruction of structural displacements, strains, stresses, and failure criteria using real-time strain measurements. Aircraft wings with embedded conformal antennas and those of *morphed* capability require real-time shape sensing to provide feedback for their actuation and control

systems. For structural health monitoring, shape- and stress-sensing technologies are the enabling capabilities for assessing structural integrity and cost-efficient maintenance. For composite and sandwich structures, structural health monitoring using embedded optical-fiber networks presents an attractive technology for in-situ strain measurements that give rise to a large amount of strain data. Despite their numerous advantages, composite structures may experience such modes of failure as delamination and impact damage, and these can affect their load carrying capabilities. Thus, the monitoring of structural integrity of multilayered composite and sandwich structures is an issue of primary importance.

Various shape-sensing approaches for plates undergoing bending deformations have been explored [1–3]. Bogert *et al.* [1] examined a modal transformation method, which requires a large number of natural vibration modes. Using classical bending assumptions, Jones *et al.* [2] performed the reconstruction of plate deflections by fitting discrete measures of the bending curvatures and then integrating the regression curves. Nishio *et al.* [3] explored shape-sensing of thin laminated composite plates by enforcing compatibility between analytic and measured strains in a weighted least-squares sense. Both [2] and [3] employed Kirchhoff plate theory, thus restricting their methods to homogeneous or nearly homogeneous thin plates. Tessler and Spangler [4] proposed a general framework for full-field reconstruction of displacements, strains, and stresses, using arbitrary positioned strain sensors on the load-carrying structural surfaces. The methodology is based on a least-squares variational principle and accounts for the complete set of First-order Shear Deformation Theory (FSDT) modes. They include stretching, bending and shear deformations. The variational principle [4] is also well suited for finite element approximations. In [5], the authors proposed an inverse Finite Element Method (iFEM) based on C^0-continuous kinematic approximations. This resulted in an efficient three-node inverse shell finite element called iMIN3.

Although generally regarded as an accurate theory, FSDT may lead to somewhat inadequate predictions when applied to relatively thick composite and sandwich structures. Higher-order equivalent-single-layer theories [6] provide improved predictions for such structures, specifically for the global response quantities such as deflection and natural frequency; nevertheless, even these theories fail to predict through-the-thickness distributions of displacements, strains, and stresses with sufficient accuracy. Layer-wise theories [7] usually lead to highly accurate response predictions; however, these are obtained at the expense of computational efficiency and modeling complexity, especially for multilayered structures, since the number of unknowns depends on the number of material layers. The recently developed Refined Zigzag Theory (RZT) [8,9] is a good compromise between adequate accuracy and computational efficiency. For plate analysis, RZT has seven kinematic variables regardless of the number of material layers, just two more than FSDT. This new theory is able to model the cross-sectional distortion that is typical of multilayered composite and sandwich structures.

In this paper, the Tessler-Spangler [4,5] iFEM formulation is reformulated to include the kinematic assumptions of RZT [8,9]. The new formulation is thus intended for applications dealing with multilayered composite and sandwich structures possessing a high degree of anisotropy and heterogeneity. The variational principle is then discretized using a C^0-continuous three-node inverse plate finite element. Numerical results are presented for moderately thick sandwich laminates subjected to various boundary and loading conditions. Finally, superior stress-sensing capabilities of the present formulation are demonstrated for a

select set of challenging material systems.

2 KINEMATIC ASSUMPTIONS OF THE REFINED ZIGZAG THEORY FOR PLATES

Herein the kinematic assumptions of the Refined Zigzag Theory (RZT) for plates are briefly reviewed. In particular, the strain field is formally re-written in order to define the *strain measures* to be used in the iFEM variational formulation (see Sect. 3).

Consider a plate of thickness $2h$ made of N perfectly bonded orthotropic material layers (see Figure 1(a)); the superscript (k) denotes the kth layer. The plate is referred to a Cartesian coordinate system (x_1, x_2, z) where (x_1, x_2) are the in-plane coordinates and z is the thickness coordinate that ranges from $-h$ to h, with $z = 0$ identifying the mid-plane and $z_{(j)}$ identifying the jth interface (see Figure 1(b)).

The displacement field of RZT for plates is [9]

$$u_1^{(k)}(x_1, x_2, z) \equiv u(x_1, x_2) + z\, \theta_1(x_1, x_2) + \phi_1^{(k)}(z)\, \psi_1(x_1, x_2) \tag{1}$$
$$u_2^{(k)}(x_1, x_2, z) \equiv v(x_1, x_2) + z\, \theta_2(x_1, x_2) + \phi_2^{(k)}(z)\, \psi_2(x_1, x_2)$$
$$u_z(x_1, x_2, z) \equiv w(x_1, x_2)$$

where $u_1^{(k)}$ and $u_2^{(k)}$ are the in-plane displacements and u_z is the transverse displacement. RZT has seven kinematic variables, $\mathbf{u} = [u, v, w, \theta_1, \theta_2, \psi_1, \psi_2]^T$. u, v, and w are the uniform displacement components along the x_1, x_2, and z-axis respectively; θ_1 and θ_2 are the average rotations of the transverse normal around the positive x_2-axis and the negative x_1-axis, respectively; and ψ_α $(\alpha = 1, 2)$ are the amplitudes of the zigzag contributions to the in-plane displacement in the x_α-directions (see Figure 1(a)). The zigzag terms $\phi_\alpha^{(k)} \psi_\alpha$ $(\alpha = 1, 2)$ in Eq. (1) describe the C^0-continuous cross-sectional distortions that are typical of multilayer laminates. The zigzag functions, $\phi_\alpha^{(k)}(z)$, have units of length and are piecewise linear, C^0-continuous functions of the thickness coordinate and of the transverse shear moduli of the laminate layers. Refer to [9] for the detailed derivation of the zigzag functions.
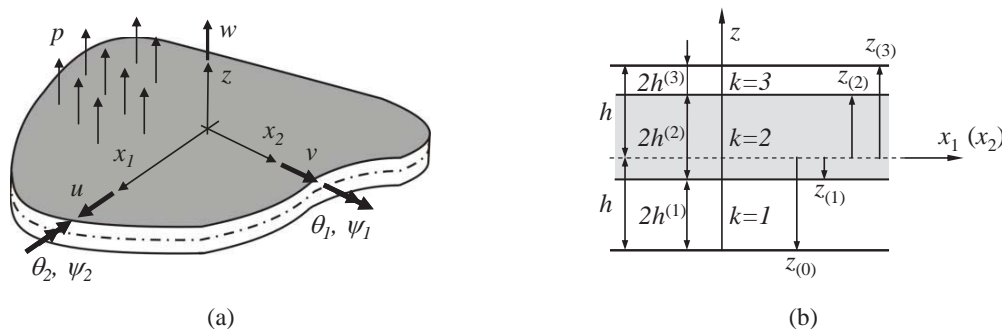

Figure 1: Plate notation (a) and layer notation for a three-layer laminate (b)

The in-plane components of the strain field are given as

$$\varepsilon_{11}^{(k)} = \varepsilon_{10} + z\kappa_{10} + \mu_{10}^{(k)} \tag{2}$$

$$\varepsilon_{22}^{(k)} = \varepsilon_{20} + z\kappa_{20} + \mu_{20}^{(k)}$$

$$\gamma_{12}^{(k)} = \gamma_{120} + z\kappa_{120} + \mu_{120}^{(k)}$$

where

$$\mathbf{e}(\mathbf{u}) \equiv \begin{Bmatrix} \varepsilon_{10} \\ \varepsilon_{20} \\ \gamma_{120} \end{Bmatrix} = \begin{Bmatrix} u_{,1} \\ v_{,2} \\ u_{,2} + v_{,1} \end{Bmatrix}, \quad \boldsymbol{\kappa}(\mathbf{u}) \equiv \begin{Bmatrix} \kappa_{10} \\ \kappa_{20} \\ \kappa_{120} \end{Bmatrix} = \begin{Bmatrix} \theta_{1,1} \\ \theta_{2,2} \\ \theta_{1,2} + \theta_{2,1} \end{Bmatrix} \tag{3}$$

$$\mathbf{m}^{(k)}(\mathbf{u}, z) \equiv \begin{Bmatrix} \mu_{10}^{(k)} \\ \mu_{20}^{(k)} \\ \mu_{120}^{(k)} \end{Bmatrix} = \begin{Bmatrix} \phi_1^{(k)} \psi_{1,1} \\ \phi_2^{(k)} \psi_{2,2} \\ \phi_1^{(k)} \psi_{1,2} + \phi_2^{(k)} \psi_{2,1} \end{Bmatrix}$$

represent the membrane, bending and zigzag strain measures, respectively. Note that, whereas the membrane and bending strain measures are constant with respect to the thickness coordinate, the zigzag strain measures have the "zigzag", z-dependent distributions.

The transverse shear strains are given by

$$\gamma_{1z}^{(k)} = \eta_1 + \left(1 + \beta_1^{(k)}\right)\psi_1 \tag{4}$$

$$\gamma_{2z}^{(k)} = \eta_2 + \left(1 + \beta_2^{(k)}\right)\psi_2$$

where $\beta_\alpha^{(k)} \equiv \phi_{\alpha,z}^{(k)}$ $(\alpha = 1, 2)$ and

$$\mathbf{g}(\mathbf{u}) \equiv \begin{Bmatrix} \eta_1 \\ \eta_1 \end{Bmatrix} = \begin{Bmatrix} \gamma_1 - \psi_1 \\ \gamma_2 - \psi_2 \end{Bmatrix} = \begin{Bmatrix} w_{,1} + \theta_1 - \psi_1 \\ w_{,2} + \theta_2 - \psi_2 \end{Bmatrix} \tag{5}$$

with η_α $(\alpha = 1, 2)$ denoting the transverse-shear strain measures of RZT.

3 INVERSE FINITE ELEMENT METHOD BASED ON RZT

In this section, the iFEM variational formulation based on the RZT kinematics is presented. The formulation enables reconstruction of the deformed shape of composite and sandwich structures from in situ strain measurements.

The general framework is that of finite element approximations. Thus, a discretization of the structure with plate elements is introduced, in which the element kinematic variables are interpolated by a set of suitable shape functions,

$$\mathbf{u}(x_1, x_2) \simeq \mathbf{u}^e = \mathbf{N}(x_1, x_2)\mathbf{q}^e \tag{6}$$

where $\mathbf{N}(x_1, x_2)$ denotes the shape functions and $\mathbf{q}^e$ the nodal degrees-of-freedom.

3.1 Error functional

Following the iFEM methodology [4,5], the displacement solution is obtained through the minimization of an error functional, which is defined as the least-square error between the analytic strain measures (Eqs. (3), (5)) and their measured values, known at discrete locations from in-situ strain measurements. For a single element, the error functional is given as

$$\Phi^e\left(\mathbf{u}^e\right) \equiv \left\|\mathbf{e}\left(\mathbf{u}^e\right)-\mathbf{e}^\varepsilon\right\|^2 + \left\|\boldsymbol{\kappa}\left(\mathbf{u}^e\right)-\boldsymbol{\kappa}^\varepsilon\right\|^2 + \left\|\mathbf{m}^{(k)}\left(\mathbf{u}^e\right)-\mathbf{m}^\varepsilon\right\|^2 + \alpha\left\|\mathbf{g}\left(\mathbf{u}^e\right)\right\|^2 \tag{7}$$

where the superscript "ε" is used to denote the measured values; for the membrane, bending and zigzag contributions, the squared norms that appear in Eq. (7) have the form

$$\left\|\mathbf{e}\left(\mathbf{u}^e\right)-\mathbf{e}^\varepsilon\right\|^2 = \frac{1}{n}\sum_{i=1}^{n}\left[\mathbf{e}\left(\mathbf{u}^e\right)_i - \mathbf{e}_i^\varepsilon\right]^2 \tag{8}$$

$$\left\|\boldsymbol{\kappa}\left(\mathbf{u}^e\right)-\boldsymbol{\kappa}^\varepsilon\right\|^2 = \frac{(2h)^2}{n}\sum_{i=1}^{n}\left[\boldsymbol{\kappa}\left(\mathbf{u}^e\right)_i - \boldsymbol{\kappa}_i^\varepsilon\right]^2$$

$$\left\|\mathbf{m}^{(k)}\left(\mathbf{u}^e\right)-\mathbf{m}^\varepsilon\right\|^2 = \frac{(2h)^2}{n}\sum_{i=1}^{n}\left[\mathbf{m}^{(k)}\left(\mathbf{u}^e,z_{(j)}\right)_i - \mathbf{m}_{i(j)}^\varepsilon\right]^2$$

where n is the number of locations $P_i = (x_1, x_2)_i$, where the strain measures, $\mathbf{e}_i^\varepsilon$, $\boldsymbol{\kappa}_i^\varepsilon$ and $\mathbf{m}_{i(j)}^\varepsilon$ are evaluated from strain-sensor measurements. The zigzag strain measures, $\mathbf{m}_{i(j)}^\varepsilon$, are evaluated at the jth interface using embedded strain-sensors. The transverse shear strain measures, $\mathbf{g}\left(\mathbf{u}\right)$, cannot be obtained experimentally. Thus, the transverse shear term in Eq. (7) is given by the L^2 norm

$$\left\|\mathbf{g}\left(\mathbf{u}^e\right)\right\|^2 = \frac{1}{A^e}\int_{A^e}\left[\mathbf{g}\left(\mathbf{u}^e\right)\right]^2 dA \tag{9}$$

where A^e denotes the element area. In Eq. (8), α is a positive valued, small (compared to unity) weighting coefficient; refer to the numerical studies in Sect. 4 in which the value of $\alpha = 10^{-5}$ is used.

Considering Eqs. (3) and (5), while invoking the kinematic field interpolations given by Eq. (6), the strain measures can be expressed in terms of the nodal degrees-of-freedom, $\mathbf{q}^e$, as

$$\mathbf{e}\left(\mathbf{u}^e\right) = \mathbf{B}_e\left(x_1, x_2\right)\mathbf{q}^e, \qquad \boldsymbol{\kappa}\left(\mathbf{u}^e\right) = \mathbf{B}_\kappa\left(x_1, x_2\right)\mathbf{q}^e \tag{10}$$

$$\mathbf{m}^{(k)}\left(\mathbf{u}^e, z\right) = \mathbf{B}_m\left(x_1, x_2, z\right)\mathbf{q}^e, \quad \mathbf{g}\left(\mathbf{u}^e\right) = \mathbf{B}_g\left(x_1, x_2\right)\mathbf{q}^e$$

where the matrices $\mathbf{B}_e$, $\mathbf{B}_\kappa$, $\mathbf{B}_m$ and $\mathbf{B}_g$ contain the derivatives of the shape functions $\mathbf{N}\left(x_1, x_2\right)$.

Substitution of Eq. (10) into Eqs.(8) and (9), and minimization of the functional Φ^e with respect to the unknown nodal degrees-of-freedom, $\mathbf{q}^e$, yields the element matrix equation $\mathbf{a}^e\mathbf{q}^e = \mathbf{b}^e$, where the matrix $\mathbf{a}^e$ is given as

$$\mathbf{a}^{e} = \frac{1}{n}\sum_{i=1}^{n}\Big[\mathbf{B}_{e}^{T}\big(x_{1},x_{2}\big)_{i}\,\mathbf{B}_{e}\big(x_{1},x_{2}\big)_{i}\Big] + \frac{(2h)^{2}}{n}\sum_{i=1}^{n}\Big[\mathbf{B}_{\kappa}^{T}\big(x_{1},x_{2}\big)_{i}\,\mathbf{B}_{\kappa}\big(x_{1},x_{2}\big)_{i}\Big]$$
$$+ \frac{(2h)^{2}}{n}\sum_{i=1}^{n}\Big[\mathbf{B}_{m}^{T}\big(x_{1},x_{2},z_{(j)}\big)_{i}\,\mathbf{B}_{m}\big(x_{1},x_{2},z_{(j)}\big)_{i}\Big] + \alpha\frac{1}{n}\sum_{i=1}^{n}\Big[\mathbf{B}_{g}^{T}\big(x_{1},x_{2}\big)_{i}\,\mathbf{B}_{g}\big(x_{1},x_{2}\big)_{i}\Big] \quad (11)$$

whereas the right-hand-side vector is

$$\mathbf{b}^{e} = \frac{1}{n}\sum_{i=1}^{n}\Big[\mathbf{B}_{e}^{T}\big(x_{1},x_{2}\big)_{i}\,\mathbf{e}_{i}^{\varepsilon}\Big] + \frac{(2h)^{2}}{n}\sum_{i=1}^{n}\Big[\mathbf{B}_{\kappa}^{T}\big(x_{1},x_{2}\big)_{i}\,\mathbf{\kappa}_{i}^{\varepsilon}\Big]$$
$$+ \frac{(2h)^{2}}{n}\sum_{i=1}^{n}\Big[\mathbf{B}_{m}^{T}\big(x_{1},x_{2},z_{(j)}\big)_{i}\,\mathbf{m}_{i(j)}^{\varepsilon}\Big] \quad (12)$$

Taking into account appropriate coordinate transformations, the element contributions are assembled into a global system of equations. Upon enforcement of problem-dependent displacement boundary conditions that prevent rigid-body motion, the inverse-problem equations take on the form

$$\mathbf{A}\mathbf{q} = \mathbf{b} \quad (13)$$

where $\mathbf{A}$ is a well-conditioned square matrix.

Equation (13) is well suited for real time applications. This is because $\mathbf{A}$ is inverted only once (assuming small displacements, the strain-sensor locations, $[(x_{1},x_{2})_{i},\pm h]$ and $[(x_{1},x_{2})_{i},z_{(j)}]$, remain unchanged.) On the other hand, the vector $\mathbf{b}$ needs to be updated at each strain-data acquisition increment. Thus, the displacement solution is efficiently computed by the vector-matrix multiplication, $\mathbf{q} = \mathbf{A}^{-1}\mathbf{b}$. The strains and stresses are readily computed for each element using strain-displacement and constitutive relations of RZT. Furthermore, strains and stresses can be used to construct failure criteria.

3.2 Evaluation of the experimental strain measures from strain-sensor data

The present method is especially aimed at structures with embedded strain sensors. In particular, a strain-sensor configuration that measures the in-plane strains is considered on the top and bottom surfaces and at one interface (refer to Eq. (2)). Considering that the zigzag contributions to the in-plane strains vanish on the top and bottom surfaces [9], the expressions for the experimental membrane and bending strain measures are derived by evaluating Eqs. (2) at the discrete locations $P_{i} = (x_{1},x_{2})_{i}$, $z = \pm h$,

$$\mathbf{e}_{i}^{\varepsilon} \equiv \begin{Bmatrix} \varepsilon_{10}^{\varepsilon} \\ \varepsilon_{20}^{\varepsilon} \\ \gamma_{120}^{\varepsilon} \end{Bmatrix}_{i} = \frac{1}{2}\left(\begin{Bmatrix} \varepsilon_{11}^{+} \\ \varepsilon_{22}^{+} \\ \gamma_{12}^{+} \end{Bmatrix}_{i} + \begin{Bmatrix} \varepsilon_{11}^{-} \\ \varepsilon_{22}^{-} \\ \gamma_{12}^{-} \end{Bmatrix}_{i} \right), \quad \mathbf{\kappa}_{i}^{\varepsilon} \equiv \begin{Bmatrix} \kappa_{10}^{\varepsilon} \\ \kappa_{20}^{\varepsilon} \\ \kappa_{120}^{\varepsilon} \end{Bmatrix}_{i} = \frac{1}{2h}\left(\begin{Bmatrix} \varepsilon_{11}^{+} \\ \varepsilon_{22}^{+} \\ \gamma_{12}^{+} \end{Bmatrix}_{i} - \begin{Bmatrix} \varepsilon_{11}^{-} \\ \varepsilon_{22}^{-} \\ \gamma_{12}^{-} \end{Bmatrix}_{i} \right) \quad (14)$$

where $\big\{\varepsilon_{11}^{+},\varepsilon_{22}^{+},\gamma_{12}^{+}\big\}_{i}$ and $\big\{\varepsilon_{11}^{-},\varepsilon_{22}^{-},\gamma_{12}^{-}\big\}_{i}$ denote the in-plane strains measured respectively at $[(x_{1},x_{2})_{i},+h]$ and $[(x_{1},x_{2})_{i},-h]$. Measuring the same strain components at the jth interface,

$\left\{\varepsilon_{11}^{j}, \varepsilon_{22}^{j}, \gamma_{12}^{j}\right\}_{i}$, and again using Eq. (2), the zigzag strain measures are determined as

$$
\mathbf{m}_{i(j)}^{\varepsilon} \equiv \begin{Bmatrix} \mu_{10}^{\varepsilon} \\ \mu_{20}^{\varepsilon} \\ \mu_{120}^{\varepsilon} \end{Bmatrix}_{i(j)} = \begin{Bmatrix} \varepsilon_{11}^{j} \\ \varepsilon_{21}^{j} \\ \gamma_{12}^{j} \end{Bmatrix}_{i} - \begin{Bmatrix} \varepsilon_{10}^{\varepsilon} \\ \varepsilon_{20}^{\varepsilon} \\ \gamma_{120}^{\varepsilon} \end{Bmatrix}_{i} - z_{(j)} \begin{Bmatrix} \kappa_{10}^{\varepsilon} \\ \kappa_{20}^{\varepsilon} \\ \kappa_{120}^{\varepsilon} \end{Bmatrix}_{i} \tag{15}
$$

Using this strain-sensor configuration, the zigzag strain measures, $\mathbf{m}_{i(j)}^{\varepsilon}$, are evaluated at the jth interface only.

4 THREE-NODE PLATE INVERSE ELEMENT BASED ON RZT

In this section, a brief description of a three-node inverse plate element is presented. The element has seven degrees-of-freedom at each node, $u_{k}, v_{k}, w_{k}, \theta_{1k}, \theta_{2k}, \psi_{1k}, \psi_{2k}$, where $k = 1, 2, 3$ is an index ranging over the three nodes. Considering that only first derivatives of the kinematic variables appear in the functional, Eq. (7), the shape functions are required to satisfy C^{0}-continuity. For this purpose, the so-called anisoparametric interpolations are used (e.g., refer to Tessler and Hughes [12] and Versino *et al.* [11]).

The in-plane displacements, bending rotations and zigzag amplitudes are interpolated using linear shape functions. The functions are defined in terms of the area-parametric coordinates L_{k} $(k = 1, .., 3)$,

$$
\chi(x_{1}, x_{2}) = \sum_{k=1}^{3} L_{k}(x_{1}, x_{2}) \chi_{k}, \quad \chi = (u, v, \theta_{1}, \theta_{2}, \psi_{1}, \psi_{2}) \tag{16}
$$

whereas a quadratic interpolation is used for the deflection

$$
w(x_{1}, x_{2}) = \sum_{k=1}^{3} L_{k} w_{k} + \sum_{k=1}^{3} \left[L_{1k}(\theta_{1k} - \psi_{1k}) + L_{2k}(\theta_{2k} - \psi_{2k}) \right] \tag{17}
$$

where the quadratic shape functions, L_{1k} and L_{2k}, are given by the expressions

$$
L_{1k} \equiv \frac{L_{k}}{2}(a_{l}L_{m} - a_{m}L_{l}) \quad L_{2k} \equiv \frac{L_{k}}{2}(b_{m}L_{l} - b_{l}L_{m}) \tag{18}
$$

$$
a_{k} \equiv (x_{1m} - x_{1l}) \quad b_{k} \equiv (x_{2l} - x_{2m})
$$

the subscripts being given by the cyclic permutation of $k = 1-3$, $l = 2, 3, 1$ and $m = 3, 1, 2$. The anisoparametric interpolations, Eqs. (16) and (17), ensure that (a) truly thin plates can be modeled without any stiffening due to shear locking, and (b) the resulting element, herein referred to as iRZT3, has the same number of degrees-of-freedom as a standard linear-interpolation element.

5 NUMERICAL EXAMPLES

A symmetric three-layer sandwich plate, with carbon-epoxy face-sheets and a PVC core is analyzed, under the action of different loadings and boundary conditions (see Table 1 for the

mechanical material properties). The thickness of each face-sheet is 10% of the total laminate thickness. In the following example problems, square plates are considered having edge length a and span-to-thickness ratios, $\rho = a/2h=10$. Regular mesh patterns are used having the same number of elements along the plate edges, n^e. Figure 2 shows the plate geometry, the coordinate system, and a 2×2 discretization ($n^e = 2$).

Two example problems are analyzed: (1) a simply supported plate subjected to a transverse bi-sinusoidal pressure $p(x_1,x_2) = p_0 \sin(\pi x_1/a) \sin(\pi x_2/a)$, and (2) a cantilever plate subjected to a uniform transverse pressure $p(x_1,x_2) = p_0$. In lieu of the actual experimental strain measurements, an exact elasticity solution by Pagano [13] is used for the simply supported plate. For the cantilever plate, an analytic RZT-based direct solution is used, [9]. In both cases, the strain sensor configuration consists of three strain-sensor rosettes located at the element centroid on top and bottom surfaces and at $z_{(1)}$ (see Figures 1 and 2).

Table 1: Mechanical properties of orthotropic (C) and isotropic (P) materials. The Young's moduli and the shear moduli are expressed in GPa.

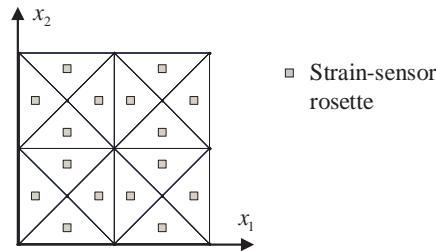| C	Carbon-epoxy unidirectional composite	$E_1^{(k)}, E_2^{(k)}, E_3^{(k)}$	1.579×10^2, 9.584, 9.584
		$\nu_{12}^{(k)}, \nu_{13}^{(k)}, \nu_{23}^{(k)}$	0.32, 0.32, 0.49
		$G_{12}^{(k)}, G_{13}^{(k)}, G_{23}^{(k)}$	5.930, 5.930, 3.227
P	PVC core	E, ν	1.040×10^{-1}, 0.3

Figure 2: Inverse plate finite element discretization, 2×2 mesh (n^e=2), and strain-sensor locations.

In Figures 3–5, the in-plane displacement, in-plane normal stress, and transverse shear stress are normalized as

$$\bar{u}_1 = u_1 \times \left(10^4 D_{11}/p_0 a^4\right), \quad \bar{\sigma}_{11} = \sigma_{11} \times \left(1/p_0 \rho^2\right), \quad \bar{\tau}_{2z} = \tau_{2z} \times \left(1/p_0 \rho\right) \tag{20}$$

where D_{11} is the bending stiffness coefficient.

Figures 3–4 depict results for the simply supported plate where the displacements and stresses obtained using the present element formulation (labeled as iRZT3) are compared to Pagano's exact elasticity solution. In Figure 3(b), for comparison purposes results are also depicted for the predecessor inverse element "iMIN3" [5], based on FSDT. When using $n^e = 12$ (Figure 3(a)), the present iRZT3 model accurately predicts the maximum deflection (error within 0.27%) whereas iMIN3 leads to an underestimation by 70% (not shown). Figures 3(b), 4(a) and 4(b) show that through-the-thickness distributions of in-plane displacement, in-plane

normal stress and transverse shear stress are accurately recovered using iRZT3 whereas iMIN3 in unable to model the zigzag shape of the in-plane displacement (Figure 3(b)) typical of a sandwich-like stacking sequence.
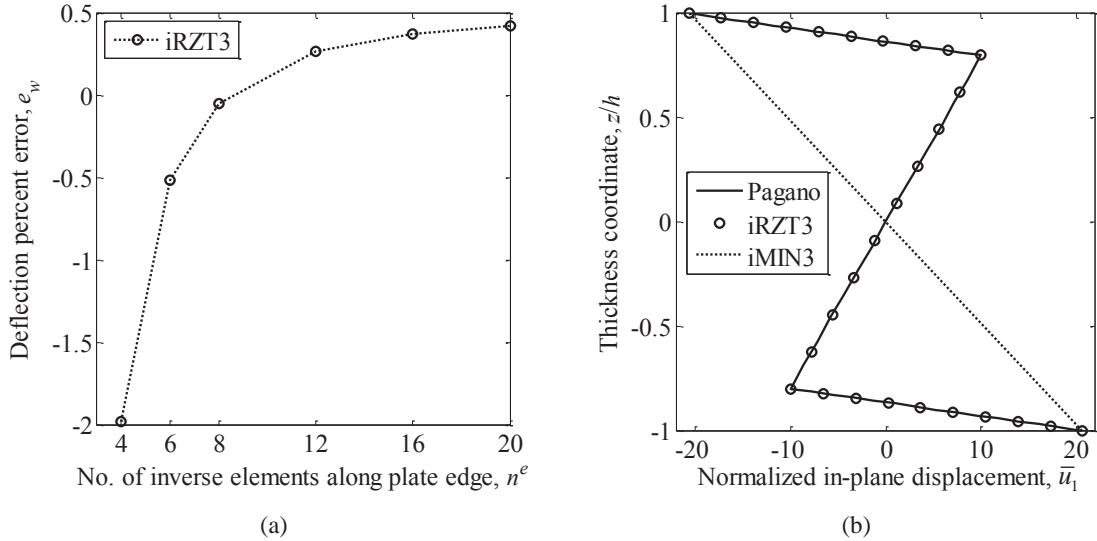

(a)

(b)

Figure 3: Simply supported plate, $a/2h$=10: (a) Percent error of maximum deflection, $e_w \equiv 100(w/w^{Pagano}-1)$, vs. the number of elements along the plate edge, n^e; and (b) Through-the-thickness distribution of in-plane displacement, $\bar{u}_1(0,a/2)$, for the discretization n^e = 12.

(a)

(b)
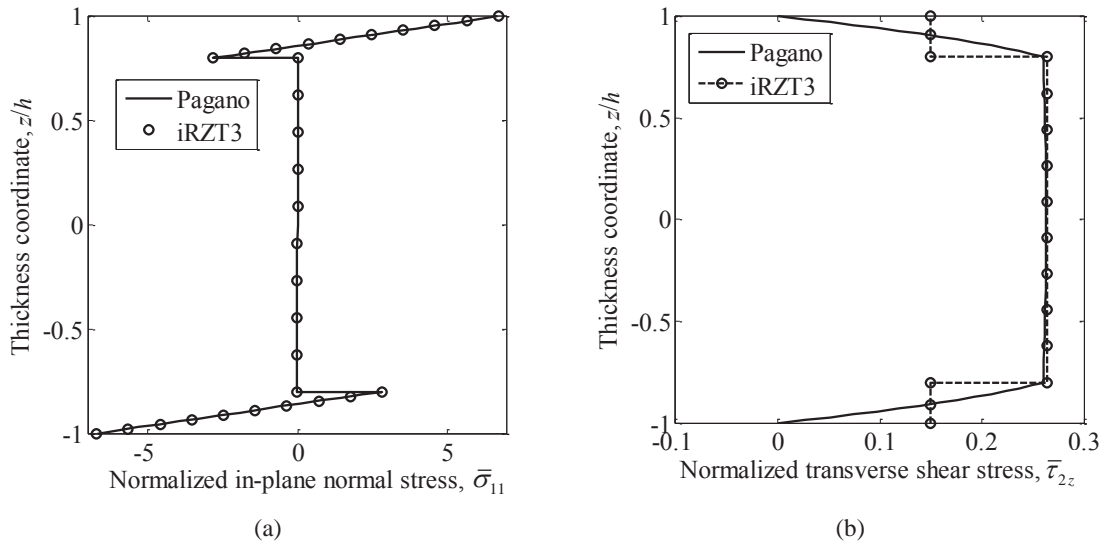
Figure 4: Simply supported plate, $a/2h$=10: through-the-thickness distributions of (a) In-plane stress, $\bar{\sigma}_{11}(a/2,a/2)$, and (b) Transverse shear stress, $\bar{\tau}_{2z}(0,a/2)$, for the discretization n^e=12.

9

In Figure 5, results are depicted for the cantilever plate, where the iFEM predictions are compared with the corresponding RZT analytic solutions of the direct problem. Figure 5(a) depicts rapid convergence of the maximum deflection error, whereas Figure 5(b) shows a through-the-thickness distribution of the normal stress, $\bar{\sigma}_{11}(a/4, a/2)$.
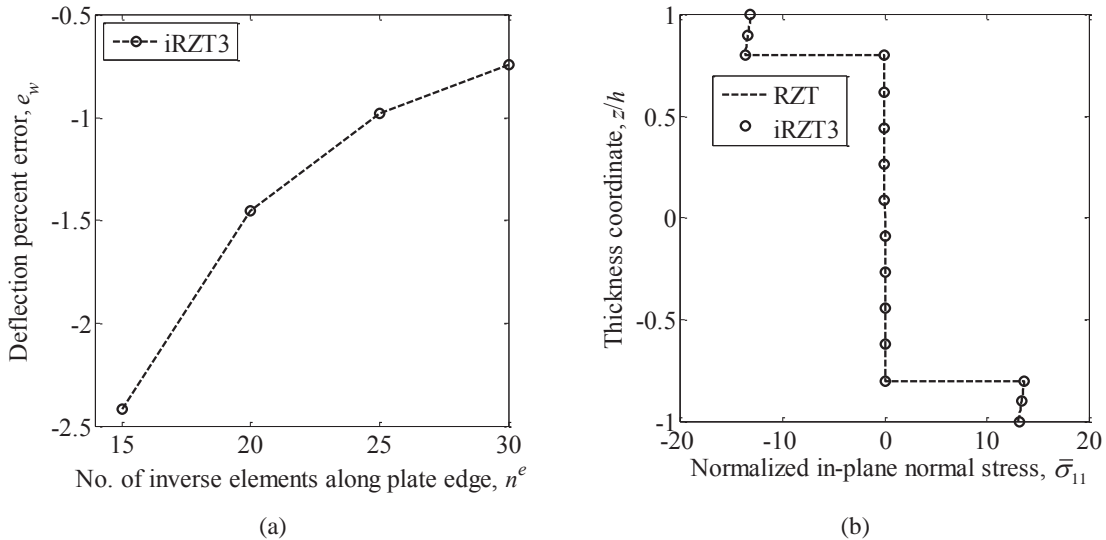

(a)   (b)

Figure 5: Cantilever plate, $a/2h$=10: (a) Percent error of maximum deflection, $e_w \equiv 100(w/w^{RZT} - 1)$, vs. the number of elements along the plate edge, n^e; and (b) Through-the-thickness distribution of in-plane stress, $\bar{\sigma}_{11}(a/4, a/2)$, for the discretization n^e=20.

6   CONCLUSIONS

Real-time reconstruction of structural displacements and stresses from in-situ discrete-location strain measurements, herein referred to as shape- and stress-sensing, is an inverse problem that has important implications for monitoring of structural integrity, as well as for the actuation and control of smart structures. A new variational formulation for shape- and stress-sensing of laminated composite and sandwich plates has been presented. The approach makes use of an inverse Finite Element Method (iFEM) that was previously developed on the basis of First-order Shear Deformation Theory (FSDT). The iFEM is based on the minimization of a least-square error functional in which analytic and measured strains are enforced in the least-square sense. Within the present formulation, the kinematic assumptions of the Refined Zigzag Theory (RZT) are used and require that the measured strains be available along three surfaces through the laminate thickness (instead of only two surfaces for the FSDT-based formulation.) The RZT has previously been shown to be especially well suited for the modeling of laminated composite and sandwich plates. The error functional is discretized using C^0-continuous interpolations of the displacement field, yielding an efficient three-node inverse plate finite element that has seven kinematic degrees-of-freedom at each node. From the reconstructed element displacements, strains and stresses at every material point of the structure are then computed using RZT's strain-displacement and constitutive

relations. Numerical results for moderately thick laminated sandwich plates undergoing elasto-static deformations demonstrated superior full-field predictions for the displacements, strains, and stresses. As expected, the present iFEM-RZT formulation results in more accurate predictions than those based on iFEM-FSDT, and this is especially evident in highly heterogeneous and sandwich laminates.

ACKNOWLEDGEMENTS

REFERENCES

[1] Bogert, P.B., Haugse, E.D. and Gehrki, R.E. Structural shape identification from experimental strains using a modal transformation technique. Proceedings of 44th AIAA/ASME/ASCE/AHS Structures, Structural Dynamics and Materials Conference, (2003), Norfolk, Virginia.

[2] Jones, R.T., Bellemore, D.G., Berkoff, T.A., Sirkis, J.S., Davis, M.A., Putnam, M.A., Friebele, E.J. and Kersey, A.D. Determination of cantilever plate shapes using wavelength division multiplexed fiber Bragg grating sensors and a least-squares strain-fitting algorithm. *Smart Mater. Struct.* (1998) **7**: 178–188.

[3] Nishio, M., Mizutani, T. and Takeda, N. Structural shape reconstruction with consideration of the reliability of distributed strain data from a Brillouin-scattering-based optical fiber sensor. *Smart Mater. Struct.* (2010) **19**: 1–14.

[4] Tessler, A. and Spangler, J.L. A least-squares variational method for full-field reconstruction of elastic deformations in shear-deformable plates and shells. *Computer Methods Appl. Mech. Engrg.* (2005) **194**: 327–339.

[5] Tessler, A. and Spangler, J.L. Inverse FEM for full-field reconstruction of elastic deformations in shear deformable plates and shells. Proceedings of 2nd European Workshop on Structural Health Monitoring, (2004), Munich, Germany.

[6] Reddy, J.N. A simple higher-order theory for laminated composite plates. *J. Appl. Mech.* (1984) **51**: 745–752.

[7] Lu, X. and Liu, D. An interlaminar shear stress continuity theory for both thin and thick composite laminates. *J. Appl. Mech.* (1992) **59**: 502–509.

[8] Tessler, A., Di Sciuva, M. and Gherlone, M. A refined zigzag beam theory for composite and sandwich beams. *J. Comp. Mater.* (2009) **43**: 1051–1081.

[9] Tessler, A., Di Sciuva, M. and Gherlone, M. A consistent refinement of first-order shear-deformation theory for laminated composite and sandwich plates using improved zigzag kinematics. *J. Mech. Mater. Struct.* (2010) **5**: 341–367.

[10] Reddy, J.N. *Mechanics of laminated composite plates. Theory and analysis*. CRC Press, Inc., (1997).

[11] Versino, D., Gherlone, M., Mattone, M., Di Sciuva, M. and Tessler A. C^0 triangular elements based on the Refined Zigzag Theory for multilayered composite and sandwich plates. *Compos. Part B-Eng.* (2013) **44**: 218–230.

[12] Tessler, A. and Hughes, T.J.R. A three-node Mindlin plate element with improved transverse shear. *Computer Methods Appl. Mech. Engrg.* (1985) **50**: 71–101.

[13] Pagano, N.J. Exact solutions for rectangular bidirectional composites and sandwich plates. *J. Compos. Mater.* (1970) **1**: 20–34.